Formation of Diverse Supercrystals from Self-Assembly of a Variety of Polyhedral Gold Nanocrystals

Ching-Wen Liao,[†] Yeh-Sheng Lin,[†] Kaushik Chanda,[†] Yen-Fang Song,[‡] and Michael H. Huang*,[†]

[†]Department of Chemistry, National Tsing Hua University, Hsinchu 30013, Taiwan
[‡]National Synchrotron Radiation Research Center, Hsinchu 30076, Taiwan

S *Supporting Information*

ABSTRACT: Cubic, rhombic dodecahedral, octahedral, and corner-truncated octahedral gold nanocrystals with sizes of tens of nanometers have been used as building blocks to form micrometer-sized supercrystals by slowly evaporating a water droplet on a substrate placed in a moist environment. Drying the droplet at 90 °C was found to yield the best supercrystals. Supercrystals were evenly distributed throughout the entire substrate surface originally covered by the droplet. Diverse supercrystal morphologies have been observed. Nanocubes formed roughly cubic supercrystals. Rhombic dodecahedra were assembled into truncated triangular pyramidal super-

crystals. Rhombic dodecahedral, octahedral, and hexapod-shaped supercrystals were generated through the assembly of octahedra. Corner-truncated octahedra formed tetrapod-shaped supercrystals at room temperature, but octahedral, truncated triangular pyramidal, and square pyramidal supercrystals at 90 °C. Nanocrystal assembly was found to be strongly shape-guided. Expulsion of excess surfactant to the surfaces of supercrystals suggests that responsive adjustment of surfactant concentration during particle assembly mediates supercrystal formation. Transmission X-ray microscopy and optical microscopy have been employed to follow the supercrystal formation process. Surprising rotational water current near the droplet perimeter carrying the initially formed supercrystals has been observed. Supercrystals appear to grow from the edge of the droplet toward the central region. Supercrystals assembled from octahedra inherently contain void spaces and possibly connected channels. The mesoporosity of these supercrystals was confirmed by infiltrating H_2PdCl_4 into the supercrystal interior and reducing the precursor to form Pd nanoparticles. The embedded Pd particles can still catalyze a Suzuki coupling reaction, demonstrating the application of these supercrystals for molecular transport, sensing, and catalysis.
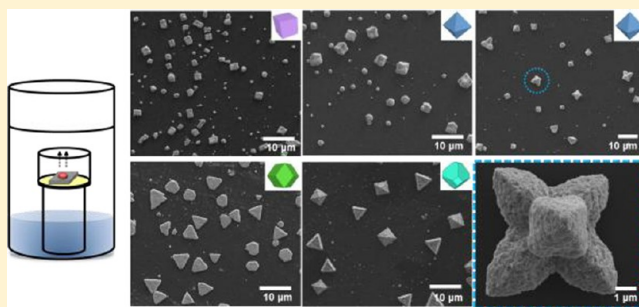
■ INTRODUCTION

Spontaneous and assisted self-assembly of inorganic nanocrystals into long-range ordered packing arrangements is a fascinating field of nanomaterials research.[1,2] A wide variety of nanoparticle superlattices constructed from spherical particles have been observed. Single and binary nanocrystal components can be assembled into unit cell structures seen in elements and binary crystals through forces and interactions among surface-functionalized molecules.[3−9] A ternary nanocrystal superlattice can also be obtained.[10] The progress in the synthesis of monodisperse polyhedral nanocrystals has enabled the fabrication of dense layered and three-dimensional packing structures from nonspherical building blocks.[11−18] An emerging research interest involving polyhedral nanocrystal assembly is the formation of supercrystals with microscale dimensions. Although some nanocrystal packing arrangements in supercrystals have been determined, less attention has been paid to the production of structurally well-defined supercrystals and the exploration of their morphological diversity.[19−22] The supercrystal formation process within an evaporating droplet and factors facilitating the generation of geometrically symmetrical supercrystals still require further examination, since layered

packing structures of nanocrystals are more typically obtained.[23] Another interesting aspect of supercrystal formation is their spatial distribution within the evaporating droplet. Furthermore, the inherent void spaces present when octahedra are orderly assembled suggest the utilization of supercrystals built from octahedral nanocrystals as three-dimensional mesoporous framework for loading, sensing, and catalytic applications.

In this study, we demonstrate the formation of supercrystals possessing diverse polyhedral structures from the organization of cubic, octahedral, corner-truncated octahedral, and rhombic dodecahedral gold nanocrystals. Remarkably, they showed well-dispersed distribution throughout the substrate. Their formation process has been recorded using optical and transmission X-ray microscopic (TXM) techniques. Local interparticle interactions including shape-guided effect and responsive adjustment of surfactant concentration among contacting particles should be operative during supercrystal formation. As a demonstration of the accessibility of the

mesopores within the octahedra-packed supercrystals, a palladium source was infiltrated and reduced to form palladium nanoparticles throughout the interior porous spaces of the supercrystals. The Pd-embedded Au supercrystals displayed catalytic activity for a Suzuki coupling reaction.

■ EXPERIMENTAL SECTION

Gold Nanocrystal Synthesis. The gold nanocrystals with various geometric shapes for assembly purposes were obtained by following the procedures developed in our laboratory.[24,25] The detailed experimental procedures are available in the Supporting Information.

Formation of Supercrystals. The volume of final gold colloidal solution was 10 mL with a cetyltrimethylammonium chloride (CTAC) concentration of 0.1 M. Then 10 mL of water was added to reduce the CTAC concentration to 5×10^{-2} M, and the solution was centrifuged. The solution with 63−70 nm gold nanocrystals was centrifuged at 3000 rpm for 10 min, while 37−43 nm nanocrystals were centrifuged at 6500 rpm for 10 min. Next, the top solution in the centrifuge tube was carefully removed to leave behind just approximately 50 μL of the concentrated particle solution, and then 50 μL of the concentrated particle solution was withdrawn and transferred to a small Eppendorf tube.

We used various polyhedral gold nanocrystals to form supercrystals in a saturated moist atmosphere by using a simple drop-casting method at room temperature or higher temperatures (60 and 90 °C). First, 1 μL of the gold colloidal solution was added to a clean silicon wafer (∼2.5 mm × 2.5 mm) or an indium tin oxide (ITO) glass. The substrate was placed over an inverted vial cap, which was placed on top of a 5-mL vial filled with 4 mL of water to prevent the vial from tilting. The 5-mL vial was placed inside a 50-mL vial with 15 mL of water added (see Figure 1). The vial was placed in an oven set at 60 or 90 °C
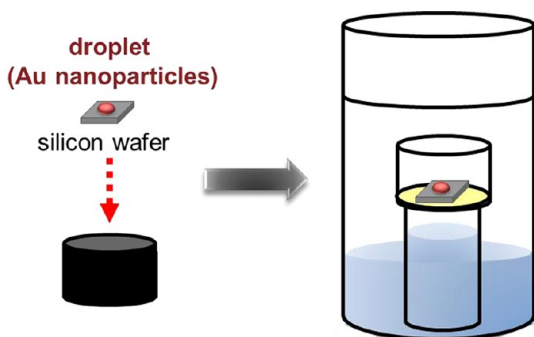

Figure 1. Schematic illustration of the setup for assembling nanocrystals by drop-coating.

to slowly evaporate the droplet. The drying time is 12 h at room temperature and 3 h at 60 and 90 °C. If the droplet was allowed to dry naturally at room temperature without the use of this closed environment, the evaporation process can end in just 20−30 min.

In-Situ Transmission X-ray Microscopy (TXM). The sample holder for TXM observation is shown in Figure S1. First, a tailor-made container was glued to an iron plate with a square opening. A Mylar polyester film was wrapped around the back side of the iron plate. The iron plate was mounted on a vertical holder, and a tiny drop of the gold nanocrystal solution (1 μL) was applied to the center of the square opening over the Mylar polyester film. Hot water was added to the lower part of the container. The added water provided a high humidity condition to reduce the rate of droplet evaporation. The nanocrystals were quickly irradiated with X-ray generated from the BL01B beamline at the National Synchrotron Radiation Research Center in Taiwan with a photon energy in the range 8−11 keV for in situ TXM imaging of the supercrystal formation process using a Princeton Instruments CCD detector.

NaOH Treatment for the Removal of Supercrystals from the Substrate. The gold supercrystals remained adherent to the silicon

substrate when subjected to a sonication treatment. To remove supercrystals from the substrate, the substrate was immersed in one drop of 0.1 M NaOH solution for 6 h. An additional drop of NaOH solution was added every 2−3 h to avoid complete drying within the 6-h period. After that, the droplet can be withdrawn and transferred to another substrate. Supercrystals maintaining their shapes were observed on the new substrate.

Preparation of Pd-Infiltrated Supercrystals. To infiltrate the void spaces of octahedra-constructed supercrystals with a Pd source and demonstrate the pore accessibility, the substrate-detached supercrystals were withdrawn and transferred to an Eppendorf tube, and then 5−10 μL of 1×10^{-4} M H_2PdCl_4 solution was introduced. The infiltration process was allowed to take place overnight. The supercrystals were washed several times with water to remove any surface Pd source. Effective removal of residual surface Pd source was confirmed by EDS analysis. Then, the Pd source inside the mesopores was reduced to Pd nanoparticles by immersing in a 0.04 M ascorbic acid solution for 3−5 h. Next, the sample was embedded in Epofix and polymerized at 40 °C for 12 h, and cut with a Reichart-Jung Oltracut E ultramicrotome for TEM analysis.

Pd-Catalyzed Suzuki Coupling Reaction. Four substrates loaded with Pd-embedded Au supercrystals were added to a mixed solution of phenylboronic acid and iodobenzene to catalyze a Suzuki coupling reaction. The detailed experimental conditions and product characterization are given in the Supporting Information.

Instrumentation. TEM characterization was performed on a JEOL JEM-2100 microscope with an operating voltage of 200 kV. SEM images of the samples were obtained using a JEOL JSM-7000F electron microscope. Optical images of the samples were obtained using an Olympus BX51 optical microscope with a digital camera attached.

■ RESULTS AND DISCUSSION

The various polyhedral gold nanocrystals used for supercrystal formation were synthesized following our previously reported seed-mediated growth procedures.[24,25] By adjusting the amount of the seed solution added to the growth solution, particle dimensions can be nicely tuned. Nanocrystals with smaller sizes of 37−43 nm were generally used in the fabrication of supercrystals, although larger particles have also been examined for their ability to form structurally well-defined supercrystals (see Figure S2 for the determination of particle sizes). High uniformity in particle shape and size is essential for their assembly into dense packing structures. A tiny droplet of highly concentrated nanocrystal solution (1 μL) with appropriate CTAC surfactant concentration was applied to a silicon wafer (∼2.5 mm × 2.5 mm), which was placed in a water-added glass vial above the water level with the vial cap tightly screwed to provide a moist environment for a slow droplet evaporation rate (Figure 1). The droplet was allowed to dry at room temperature for 12 h or at higher temperatures (60 and 90 °C) by placing the vial in an oven for 3 h.

Low-magnification SEM images show extensive production of supercrystals with largely sizes of a few micrometers scattered uniformly over the entire substrate surface initially covered by the droplet (see Figure 2). The supercrystals were formed at a drying temperature of 90 °C from assembly of the smaller-sized nanocrystals. Remarkably, essentially all the nanocrystals have been incorporated into the supercrystals, giving a fairly clean substrate appearance. Nanocubes were assembled into supercrystals with cubic and rectangular shapes. Rhombic dodecahedra packed into triangular and hexagonal platelike morphologies. Octahedra can form supercrystals with rhombic dodecahedral, octahedral, and exotic hexapod structures, although rhombic dodecahedral supercrystals were more frequently observed. Octahedral supercrystals were
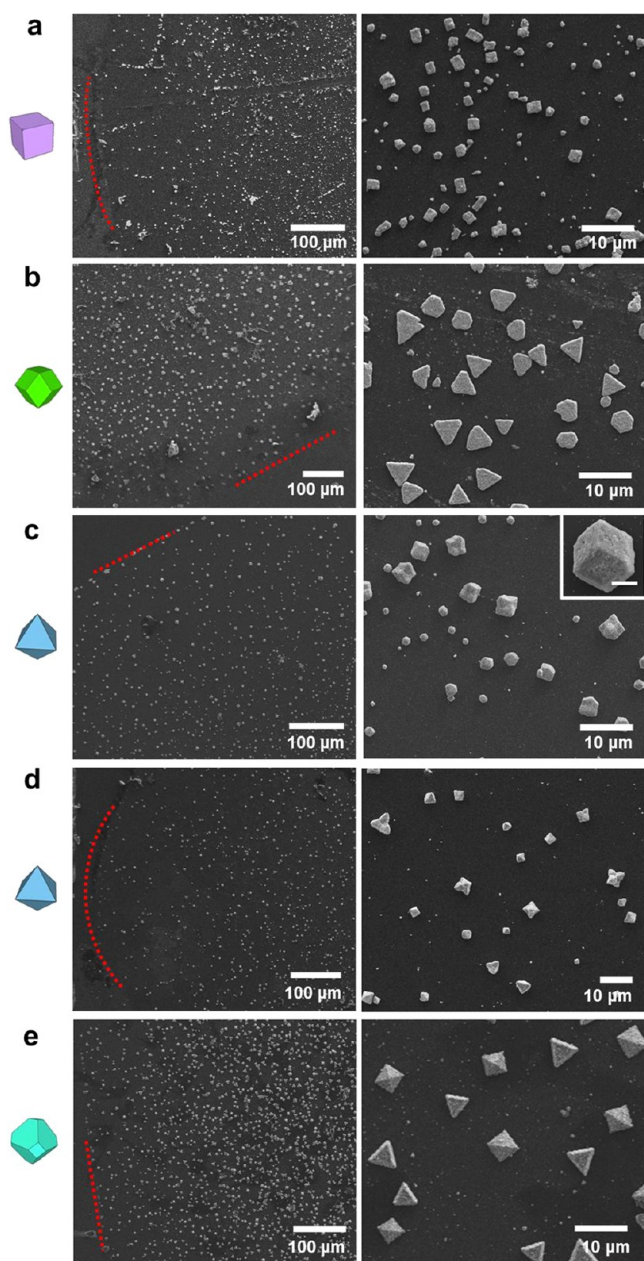
Figure 2. Supercrystals evenly scattered over the entire substrate surface covered by an evaporating droplet. (a−e) Ultralarge-area SEM images showing that supercrystals are evenly distributed throughout the entire substrate surface initially covered by the concentrated nanocrystal droplet. Cubic, rhombic dodecahedral, octahedral, and corner-truncated octahedral gold nanocrystals were assembled in a moist atmosphere to form these supercrystals at 90 °C. Two distinct supercrystal structures constructed from octahedra are shown. Right panels display SEM images of individual supercrystals around the central region of the evaporating droplet to reveal their geometric shapes. Inset shows magnified SEM images of a single supercrystal. Scale bar is 1 μm for the inset image.

water evaporation process. Instead, most of the particles are likely aggregated in the vicinity of their initial positions when the droplet is applied. The nanocrystal aggregation or ordered assembly process begins very quickly in the bulk liquid at the early stage of the evaporation time period, while evaporation-induced liquid flow is much slower. The initially formed supercrystals are sufficiently large and heavy that they resist movement over substantial distances to the droplet edges, and continue to grow in a more localized fashion by rapidly incorporating surrounding nanocrystals into the supercrystals, resulting in uniform dispersion of supercrystals on the substrate. Suppression of the coffee-ring effect, in which colloidal particles are concentrated around the perimeter when a drop of liquid is dried, through the use of micrometer-sized ellipsoidal polystyrene particles, has been demonstrated.[26] Here we show that formation of micrometer-sized supercrystals from self-assembly of nonspherical polyhedral nanocrystals can also prevent emergence of the coffee-ring effect.

SEM images of a wide variety of supercrystals produced from dense packing of these polyhedral gold nanocrystals at different droplet evaporation temperatures are provided in Figure 3. Large-area SEM images of these supercrystals formed at room temperature and 90 °C reveal their similarly dense but well separated distribution on substrates (Figure S3). Although supercrystals can usually be obtained at room and higher temperatures, a droplet evaporation temperature of 90 °C has been found to yield supercrystals with the best quality in terms of structural perfection. Substrate surface is also much cleaner at this temperature practically without observation of scattered or layered assembly of individual nanocrystals. Thus, higher temperatures should increase nanocrystal motion in the bulk liquid and enhance their incorporation into the growing supercrystals. The nanocubes showed extensive monolayer and multilayer packing structures on substrates along with the formation of supercrystals at room temperature and 60 °C. Examination of the entire substrate surface by SEM and optical microscopy revealed drastically different manners of nanocube assembly at room temperature and 90 °C (Figure 4). While supercrystals are evenly scattered over the entire droplet-deposited area on the substrate at 90 °C (see Figure 2a, Figure 4a, and Figure S3a), supercrystals are observable only near the edge of the droplet with less regular shapes at room temperature (Figure 4c). The most striking feature of nanocube assembly at room temperature is that they formed a nearly continuous film on the substrate with multilayer packing of nanocubes over the vast central region and monolayer packing around the droplet perimeter (Figure 4b). A major reason for this peculiar nanocube assembly behavior is because contacting nanocubes are less tightly packed, whereas for other particle shapes the particles are locked in position to restrict movement once they are assembled. Interestingly, the formation of a continuous multilayer film also shows that most nanocubes are not carried toward the droplet edge during droplet evaporation despite their weaker interlayer anchoring strength. The result further suggests that particle assembly takes place quickly and extensively over the entire substrate surface to form multi-layered packing locally. Only nanocubes initially located near the droplet edge can form 3-dimensional (3-D) supercrystals due to greater particle motion in this region induced by a higher liquid flow rate (see discussion of Figure 7).

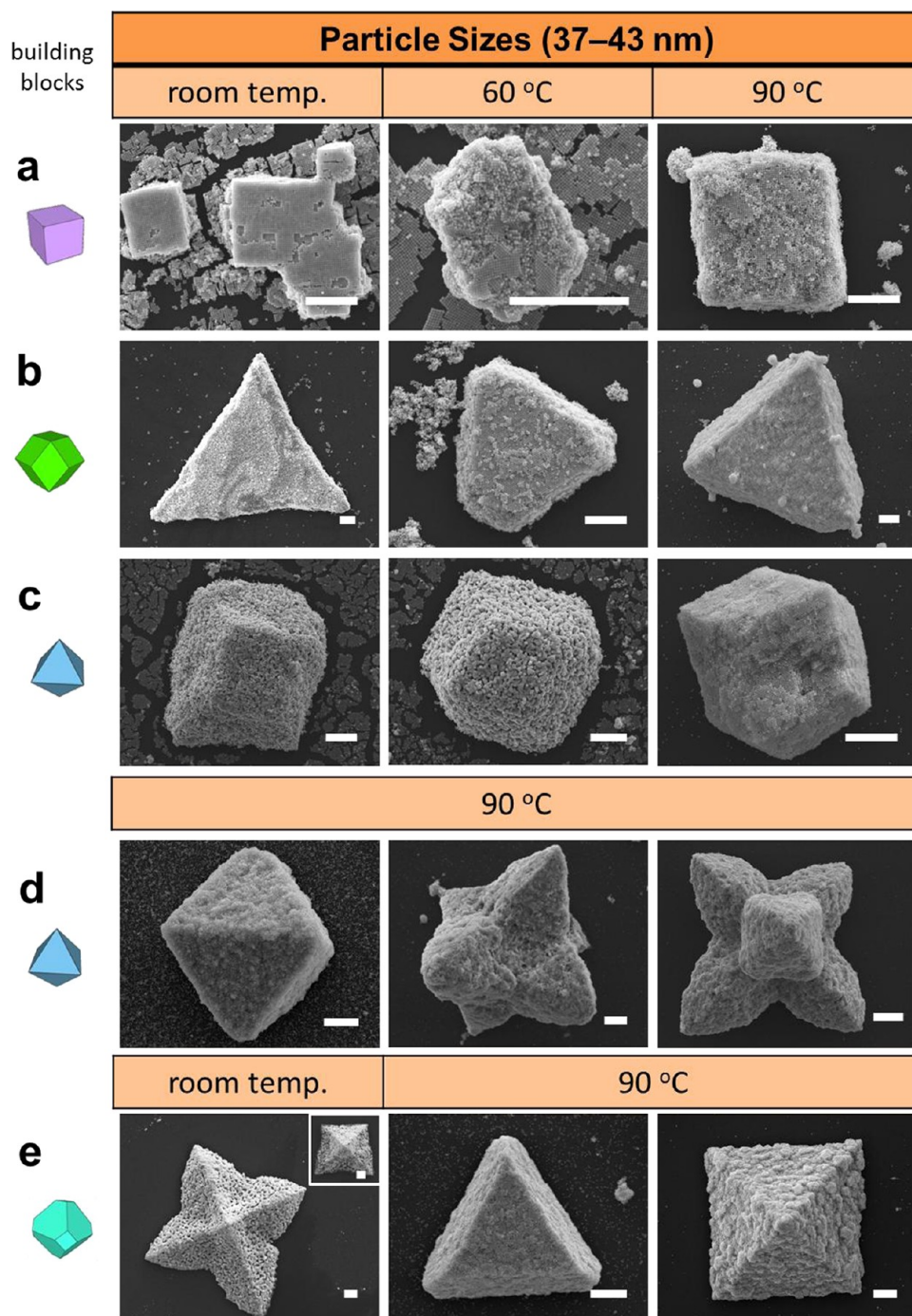Rhombic dodecahedral gold nanocrystals form supercrystals with stretched triangular and tripod morphologies and their

generated from the self-assembly of corner-truncated octahedra. Thus, supercrystals possessing diverse geometric structures can be generated from various polyhedral nanocrystal building blocks. The fact that supercrystals are evenly distributed throughout the entire substrate surface covered by an evaporating droplet indicates that most of the nanoparticles did not flow toward the droplet perimeter during this slow

Figure 3. Supercrystals formed from various nanocrystal building blocks. (a−e) Supercrystals possessing diverse geometric shapes have been generated from the assembly of various polyhedral gold nanocrystals. Supercrystals with a higher degree of structural perfection were generally obtained at a droplet evaporation temperature of 90 °C. Scale bars are equal to 1 μm.

structural variations at room temperature (Figure 3b and Figure S3b). The tripod shape is an unusual supercrystal structure not reported before. Substrate surface also appears relatively clean. At higher temperatures, especially at 90 °C, truncated triangular pyramidal supercrystals with flat top faces were more frequently observed, although some thick hexagonal platelike supercrystals were also produced. Octahedral gold nanocrystals typically form supercrystals with a rhombic dodecahedral geometry (Figure 3c). Partially fused rhombic dodecahedral supercrystals have been synthesized at room temperature and 60 °C (also see Figure S4), but supercrystals without particle fusion can be

more readily obtained at 90 °C. The formation of these fused structures should be attributed to oxidation of the octahedral gold nanocrystals in the initially formed supercrystals by dissolved oxygen to form $AuCl_4^-$ ions, and subsequent reduction back to gold atoms by possibly hydroxide ions in water. These reactions should take place slowly but continuously. The possibility of iodide, introduced in the synthesis of octahedra and corner-truncated octahedra, acting as a possible reductant can be eliminated due to its trace amount in the solution. Also, gold nanoparticles were not formed by mixing $HAuCl_4$ and KI in water. The slow water
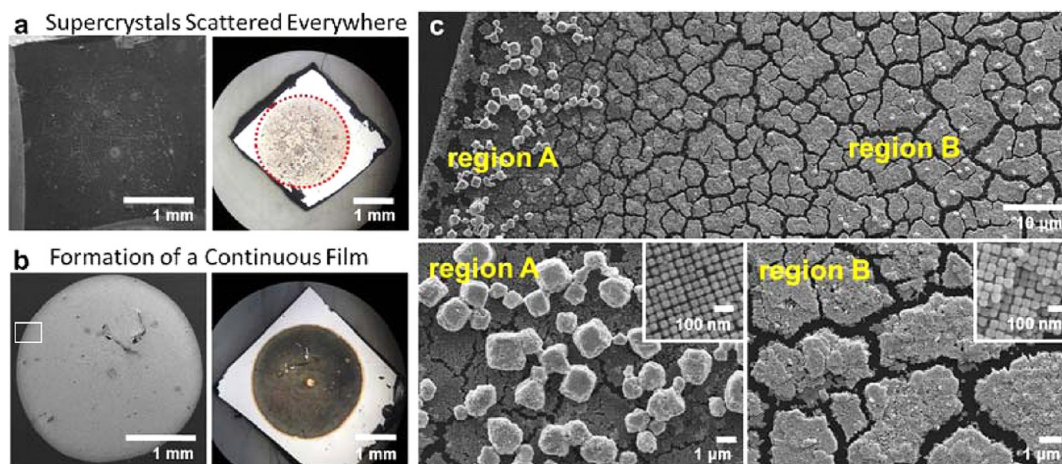
Figure 4. Two patterns of nanocrystal assembly observed. (a) SEM and optical images showing the entire area of the droplet on a silicon wafer. The droplet size is about 2 mm, as indicated by the red dotted circle. Supercrystals assembled from the 38–40 nm nanocubes at 90 °C are evenly scattered over the entire deposited area. The same phenomenon was observed for supercrystals assembled from other particle shapes. (b) SEM and optical images showing the entire area of the droplet on a silicon wafer. Here the 38–40 nm nanocubes formed a continuous film at room temperature. (c) SEM images of the rectangular region in panel b. Two distinct nanocrystal assembly regions can be identified. In region A near the droplet edge, supercrystals were formed. Beneath the supercrystals, a monolayer packing of nanocubes was observed, as seen in the inset image. In region B or the vast central region, multilayer assembly of nanocubes was observed (see the inset image). Cracks formed when solution was completed dried.

evaporation rate under a moist environment provides the time needed for significant fusion process to occur; orderly packed octahedra without fusion can be readily achieved by evaporating a drop containing octahedral gold nanocrystals in open air at room temperature.[25] At 90 °C, there should be less dissolved oxygen in the droplet, and water evaporation also proceeds faster to minimize particle fusion. The fact fused structures are only observed in supercrystals assembled from octahedra and corner-truncated octahedra suggests that the Au {111} faces are more susceptible to oxidation. Fused structures can often be observed in aqueous solutions containing gold nanoparticles, including octahedral gold nanocrystals, after long-time storage, and many nanoparticles possess the {111} surfaces. The partially fused supercrystals are quite interesting because they are porous gold crystals that can be easily fabricated for sensing and catalytic applications.[27]

Octahedral gold nanocrystals can also assemble to form supercrystals with octahedral and hexapod structures at 90 °C (Figure 3d). The hexapod structure can be considered as derived from a cuboctahedron with each of its six square faces growing to form a short square rod, which terminates with a tapered tip. Cu$_2$O and Ag$_2$O crystals have been reported to exhibit this complex but highly symmetrical structure.[28,29] Interestingly, supercrystals assembled from corner-truncated octahedra at room temperature adopt a structural variation of the hexapods with only four branches formed (Figure 3e). The bottom faces of the tetrapods are flat (see the upper left corner of Figure S3e for an inverted tetrapod). Some supercrystals have less developed arms (Figure 3e, inset), while others form more separated branches or arrowheads (Figure S3e). At 90 °C, supercrystals with truncated triangular pyramidal and square pyramidal shapes were produced from the assembly of corner-truncated octahedra. Finally, when larger nanocrystals with sizes of 63–70 nm were used for particle assembly, structurally well-defined supercrystals were harder to obtain for cubes and rhombic dodecahedra (Figure S5). Supercrystals with a rhombic dodecahedral geometry can still be generated from the dense packing of octahedra at 90 °C. Corner-truncated

octahedra also formed truncated triangular pyramidal and octahedral supercrystals at 90 °C.

Fine details of the nanocrystal packing arrangements in some supercrystals are shown in Figure 5. Nanocubes make exact face-to-face contacts throughout an entire supercrystal. Another packing manner observed at high drying temperatures is that the positions of adjacent upper and lower layers of nanocubes are shifted, such that a nanocube sits at the crossed point of four cubes in the lower layer (Figure S6). The fact that nanocubes can assemble into this alternate layer packing arrangement suggests that variation of solvent drying temperature may be used to extend the variety of superlattice structures. The relatively weak interlayer interactions among the nanocubes also contribute to these stacking manners. A third type of nanocube packing, found in the multilayer region at 90 °C, has the same alternate stacking arrangement, but nanocubes are widely separated with a gap of ~9 nm (Figure S6). This distance is much longer than the surfactant bilayer (32 ± 2 Å determined for cetyltrimethylammonium bromide bilayer thickness with partial interdigitation).[30] Again the high temperature may supply particles with energy to adopt a more loosely packed superstructure. Rhombic dodecahedra only form one type of packing arrangement with each of their 12 faces contacting neighboring particles. They align with their 3-fold axes oriented perpendicular to the substrate plane. Computer simulation of a dense packing arrangement formed by rhombic dodecahedra yielded noncontacting particles with a coordination number of ~15.[31] Noncontacting cubes have been generated when conditions of localized defects are considered.[32] Locally jammed packing structures can also appear in simulations of densest packings by polyhedra.[33] The outcomes are not necessarily consistent with experimental observations partly because surfactant is critical to nanocrystal assembly, but this factor is missing in the simulation. Octahedra essentially form only one stable 3-D packing arrangement, in which all eight faces of an octahedron make partial contacts with neighboring octahedra.[15] This is the most space-efficient and stable packing structure for octahedra, because individual
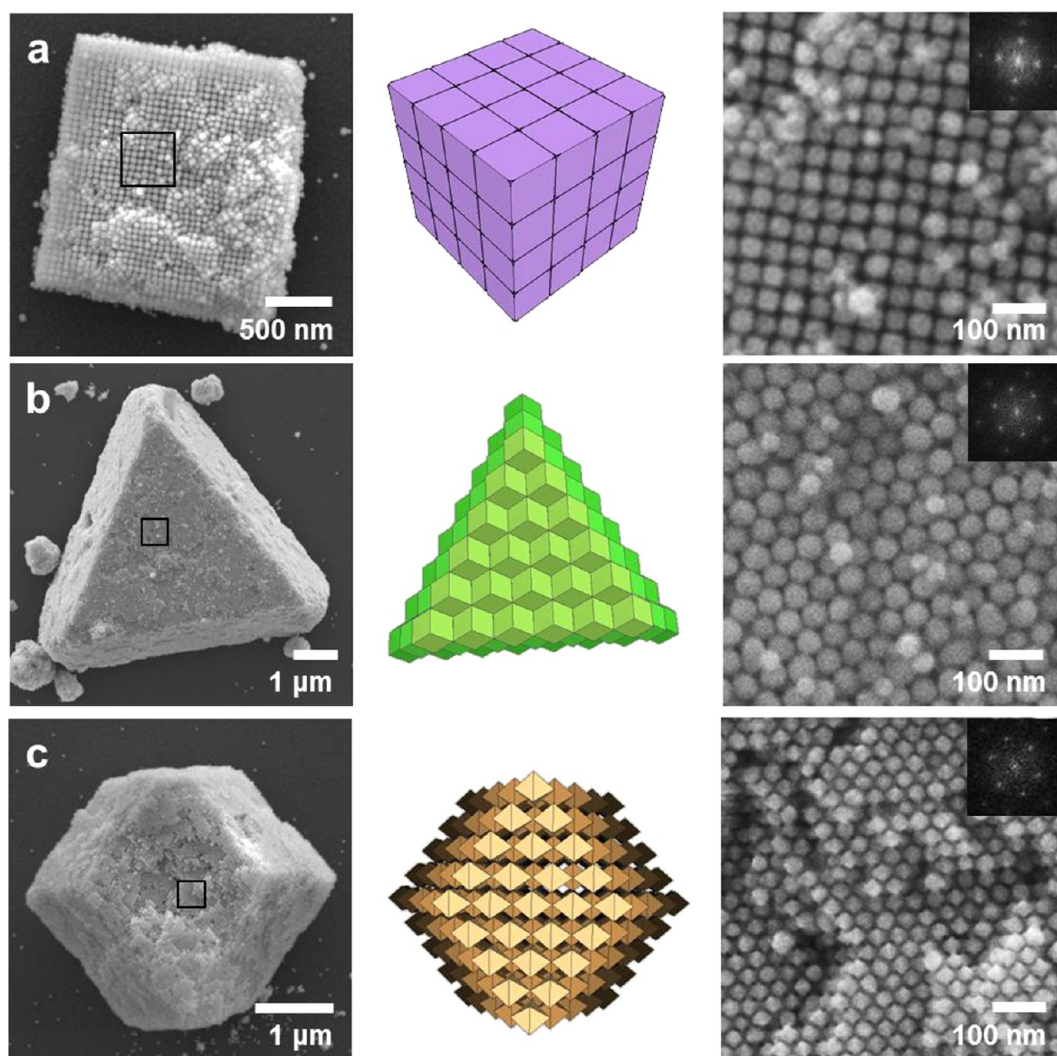
Figure 5. Nanocrystal packing structures within single supercrystals. (a–c) SEM images of single supercrystals and high-magnification SEM images of the marked square regions showing nanocrystal packing arrangements. Models of supercrystals constructed from cubic, rhombic dodecahedral, and octahedral gold nanocrystals show the same orientation as the supercrystals seen in the SEM images. Insets show the corresponding Fourier transform patterns over the central regions of single supercrystals.
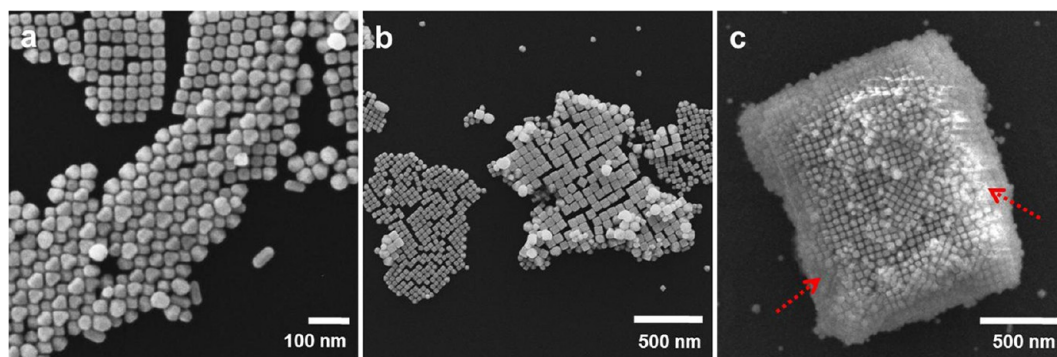

Figure 6. (a, b) SEM images showing the shape-guided effect in nanocrystal assembly. Byproducts sometimes observed in the synthesis of gold nanocubes with pentagonal projection were found to assemble into their own packing structure, while the nanocubes also formed their monolayer assembly. When a mixture of gold nanocubes with two different sizes was intentionally used for particle assembly, the larger and smaller nanocubes formed their own packing structures. (c) SEM image of a supercrystal built by assembly of nanocubes. The brightly white and surrounding blurry gray effect during SEM imaging, as indicated by the arrows, results from surface deposition of surfactant. Electron charging effect from nonconducting surfactant produces the brightly white contrast.

particles are locked tightly in position. They can show different orientations of deposition on the substrate with their faces,

edges, or corners oriented vertically with respect to the substrate surface (Figure 5c and Figure S7), or assemble into
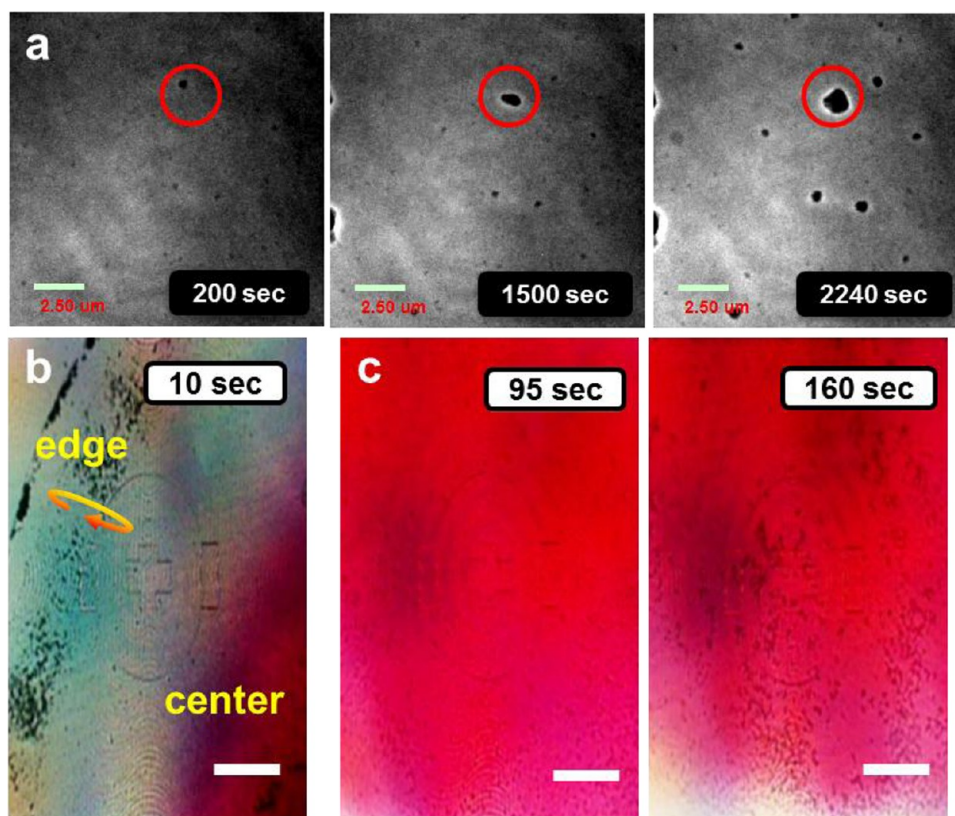
Figure 7. In-situ TXM and optical microscopy observation of the supercrystal formation process in the droplet. (a) Selected TXM images recorded to show the growing size of supercrystals using 40-nm rhombic dodecahedral nanocrystal building blocks. The initially formed supercrystals showed slightly drifting motion in the solution beyond 900 s. The red circle marks the same area on the substrate. The supercrystals appeared fixed on the substrate and grew more rapidly between 1500 and 2240 s before the droplet is dried. The drying time is about 38 min. (b) Optical microscopic image of the edge portion of a droplet 10 s after the drop was added to the same TXM sample stage with a Mylar polystyrene film for real-time observation. The arrow indicates the rapid rotational motion of nanocrystal aggregates assembled from rhombic dodecahedra. The oval and cross patterns are marks on the sample stage of the microscope and can be ignored. (c) As time proceeds, the purplish red solution color gradually recedes toward the central region of the droplet. Many more nanocrystal-assembled structures are observed around the white background region at 160 s than at 95 s. The droplet drying time is about 10 min without a humid environment. Scale bars are equal to 100 μm for optical images.

different supercrystal morphologies including rhombic dodecahedral, octahedral, and hexapod shapes (Figure S8). Corner-truncated octahedra display the same dense 3-D packing arrangement as octahedra. Octahedral supercrystals with various orientations are scattered around the edge of the droplet, while truncated triangular pyramidal and square pyramidal supercrystals reside in the vast central region (Figure S9).

Optical properties of the triangular platelike supercrystals assembled from 37−40 nm rhombic dodecahedral gold nanocrystals on an indium tin oxide (ITO) glass were examined (Figure S10). Due to their extremely large dimensions on the order of several micrometers or more, the supercrystals display a golden color with metallic luster. At these sizes, the characteristic purplish red color of dispersed nanocrystals from their surface plasmon resonance (SPR) absorption disappears. This optical feature can be used to monitor the formation of supercrystals.

The fact supercrystals are evenly scattered over the entire substrate surface covered by the evaporating droplet, rather than concentrated around the edge, shows that a better understanding of the supercrystal formation process and factors affecting the nanocrystal assembly is necessary through direct experimental observation. In the synthesis of gold nanocubes, polyhedral nanocrystals with an asymmetric pentagonal

projection were sometimes prepared as byproducts. Nanocubes and the polyhedral byproducts form their own assembly patterns (Figure 6a). This phenomenon manifests that self-assembly of polyhedral nanocrystals is strongly shape-guided; particles possessing different shapes are excluded. Furthermore, when a droplet containing nanocubes with two very different sizes was applied to a substrate, the larger and smaller nanocubes also form their own assembled structures (Figure 6b). The implication of these observations is that interparticle forces or interactions are strongest or most favorable when nanocrystals of the same size and shape are assembled. Another important insight arises from SEM analysis of supercrystals. If supercrystals were not washed by adding a drop or two of water to remove some surfactant, the excess surfactant present on the surface of a supercrystal can produce a charging effect with bright spots and a hazy image surrounding the supercrystal (Figure 6c). This observation suggests that excess CTAC surfactant molecules are expelled from the supercrystal as nanocrystals are assembling into a dense packing structure. This behavior is reasonable and is driven by the need to form a thermodynamically stable state of interdigitated bilayer of surfactant between contacting nanocrystals. This responsive adjustment of surfactant concentration between particles during their self-assembly may be operative or sensed over long ranges. The exceptionally long-range balance of interparticle forces
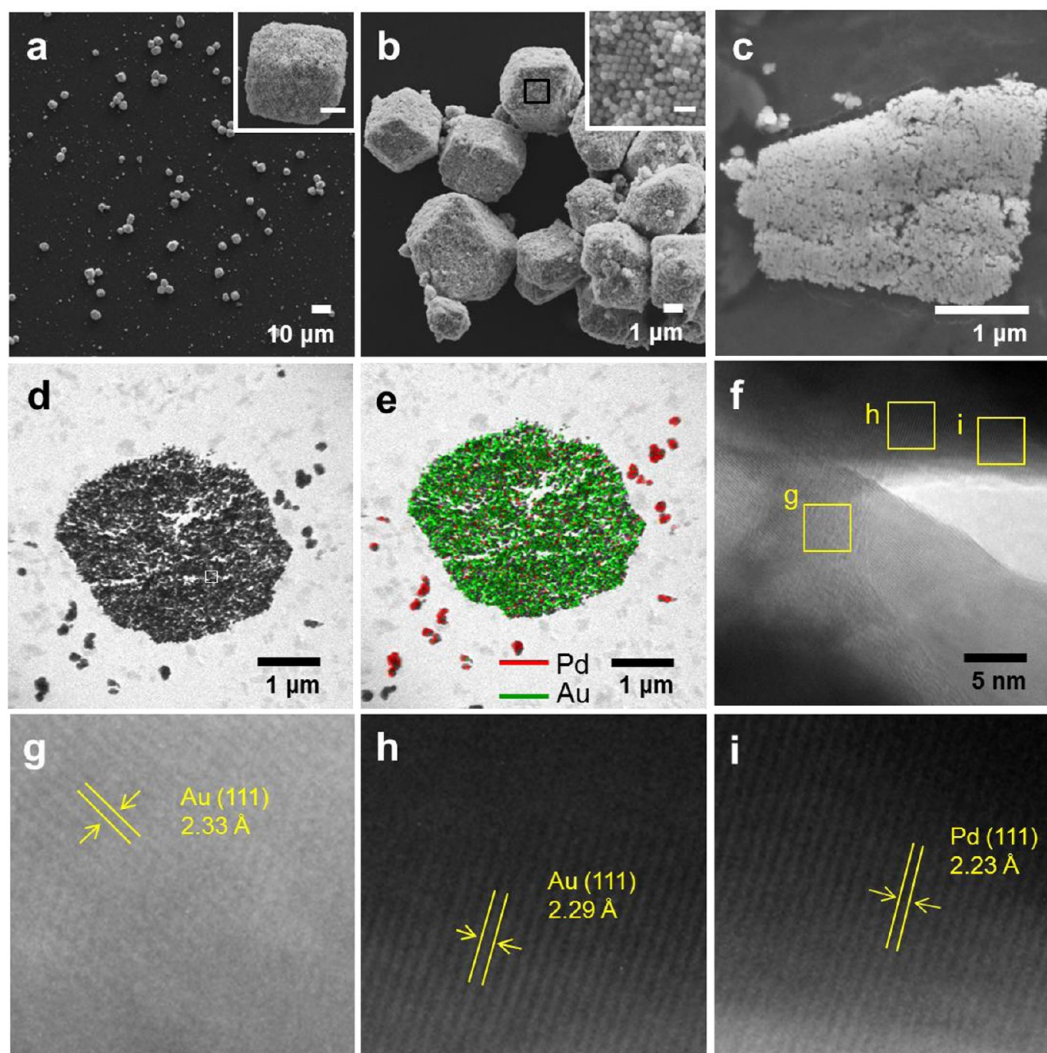
Figure 8. Demonstration of mesoporosity within the supercrystals. (a) SEM image of octahedra-assembled gold supercrystals with a rhombic dodecahedral geometry before treatement with NaOH solution. Inset shows a magnified SEM image of a single supercrystals. Scale bar is equal to 1 μm. (b) SEM images of the supercrystals after NaOH treatment and transfer to another substrate. Inset gives SEM image of the square region with a scale bar equal to 100 nm. (c) SEM image of a microtomed slice of a supercrystal after substrate transfer. (d, e) TEM and EDS elemental mapping images of a microtomed thin film from an octahedra-assembled supercrystal after the formation of Pd nanoparticles. (f) HR-TEM image of a portion of the microtomed supercrystal shown in panel d. (g–i) HR-TEM images of marked square regions shown in panel f. Lattice fringes corresponding to the Au (111) and Pd (111) lattice planes have been determined.

from all directions during the surfactant-mediated nanocrystal assembly enables the formation of supercrystals with highly symmetric geometry. This surfactant-directed assembly is similar to the cooperative interactions between inorganic molecular species and surfactant in the fabrication of mesostructured silica.[34] This long-range globally balanced state may also account for the generation of mesoporous carbon and silica crystals with rhombic dodecahedral and other polyhedral structures.[35,36]

The process of nanocrystal assembly has been considered to be entropy-driven. The obvious entropy increasing process is water evaporation. However, supercrystals appear to have been formed in the bulk solution of the droplet before its evaporation. Formation of surfactant-templated mesostructured silica is also achieved in a bulk solution. Thus we consider the responsive organization of surfactant to achieve the minimum energy of the system as the major driving force for nanocrystal assembly and the formation of supercrystals. This includes the response to the different shapes and sizes of contacting nanocrystals resulting in separated assembly. It is not easy to conceive why a highly organized nanocrystal and surfactant arrangement should lead to an increase in entropy. Since the process of supercrystal formation is spontaneous under the current reaction conditions, surfactant organization within the supercrystals should represent a more thermodynamically stable state relative to a state of randomly dispersed particles with capping surfactant. Nanocrystal assembly is considered an energy-stabilization process and is energetically favorable. This decreases the enthalpy, so ΔH is negative and the free energy change (ΔG) is also negative within a large temperature range.

TXM microscopy has been employed to record the entire supercrystal formation process. This imaging technique was previously used to monitor the hollowing process of Cu_2O–Cu_2S core–shell cubes and octahedra.[37] Hot water was added below the nanocrystal droplet to mimic the moist environment used in the production of supercrystals (Figure S1). Figure 7a shows some snapshots in the growth of supercrystals from the assembly of rhombic dodecahedral gold nanocrystals (also see

the Supporting Information movies). Small supercrystals are formed at the very early stage of the drying process. They appear to increase their sizes slowly for a long period of time, and more rapidly near the final minutes of the water evaporation process. Significant size growth can be easily recognized in the period of 25 and 37 min. The droplet dried completely after 38 min. Optical microscopy observation of the supercrystal formation process using the rhombic dodecahedral nanocrystals revealed even more remarkable phenomena. A droplet was allowed to dry in ambient environment. Large particle aggregates, possibly the initially formed supercrystals, were already visible within seconds after the droplet was applied to a Mylar polystyrene film serving as the transparent support (Figure 7b). Surprisingly, these supercrystals were found to make constant rotational motion in a belt around the perimeter of the droplet. The presence of this rotational current flow means that nanocrystals near the edges are more likely to assemble in the bulk solution of the droplet, rather than on the substrate surface. The phenomenon also explains why cubic supercrystals are mostly observed near the droplet edge, and why the corner-truncated octahedra-assembled octahedral supercrystals showing different orientations of deposition are more easily found at the droplet edge. Away from the droplet edge, the characteristic purplish red color from the SPR light absorption of dispersed nanocrystals is visible. Large supercrystals can be seen in this region (the black color). This shows that the majority of the particles are not transported to the droplet edge. Interestingly, the purplish red solution color gradually recedes toward the central region of the droplet, and more supercrystals are found scattered everywhere. Supercrystals are initially more confined at the edge of the red circle (lower portion of the image taken at 95 s), and become permeated toward the central region at a later time (160 s). The receding purplish red color and the increasing number of supercrystals observed suggest that nanocrystals are quickly incorporated into the growing supercrystals, and that their growth generally starts from the edge to the central region. These new insights show that long-range forces and interactions are as important as interparticle forces, and forces at different scales should be considered to give a more complete picture of supercrystal formation.

As Figure 5 suggests, supercrystals assembled from octahedra should contain many void spaces and connected nanoscale channels, despite the presence of surfactant. They are possibly the best materials for the initial investigation of mesoporosity in supercrystals. To visually confirm the accessibility of these porous structures, we attempted to load palladium precursor (H_2PdCl_4) into the interior of the supercrystals and reduce them to Pd nanoparticles for cross-sectional TEM examination. It is obviously desirable if the supercrystals can be removed from the substrate without structural deformation for TEM analysis and other applications. The supercrystals remained structurally stable and fixed to the substrate when subjected to a sonication treatment, which is necessary for their electrochemical applications. We found immersion of the supercrystals in a drop of 0.1 M NaOH solution for 6 h can remove and transfer them to another substrate (Figure 8a,b). The suspended supercrystals can then be sliced to thin films by microtome. SEM image of a sliced supercrystal shows that individual nanocrystals are still discernible (Figure 8c). After the infiltration of the Pd precursor into the supercrystal pores, surface Pd precursor was washed away, and the interior precursor was reduced by ascorbic acid to form Pd nano-

particles. Effective removal of surface Pd precursor has been confirmed by EDS analysis of washed supercrystals (Figure S11). TEM image and the corresponding elemental mapping of a sliced thin film of the supercrystal reveal uniform distribution of palladium throughout the interior of the supercrystal (Figure 8d,e). Pd nanoparticles were found to randomly deposit on the gold surface with the same lattice fringe orientations as the nearby gold (Figure 8f–i). To further demonstrate the pore accessibility, the Pd-infiltrated Au supercrystals were used to catalyze a Suzuki coupling reaction between iodobenzene and phenylboronic acid at 105 °C. The reaction was still not completed even after 24 h of reaction with only 35% of biphenyl product formed (Figure S12). In contrast, the Suzuki coupling reaction was completed in 10 h when supercrystals containing both exterior and interior Pd nanoparticles were used. The slow reaction progress is due to the limited diffusion of the reactant molecules into the supercrystal interior. The results show that the interior spaces of these supercrystals are accessible to molecular transport for demonstration of their various applications.

■ CONCLUSION

Cubic, rhombic dodecahedral, octahedral, and corner-truncated octahedral gold nanocrystals have been used as building blocks to form micrometer-sized supercrystals by slowly evaporating a water droplet on a substrate placed in a moist environment. Supercrystals were evenly distributed throughout the entire substrate surface, rather than concentrated around the droplet perimeter. Diverse supercrystal morphologies were produced. Transmission X-ray microscopy and optical microscopy were used to monitor the supercrystal formation process. Surfactant is believed to mediate the supercrystal assembly process, and the formation of supercrystals is an energy minimization process and favorable under a slow solvent evaporation condition. Spontaneous self-assembly of particles of the same size and shape may also be driven by surfactant-mediated interparticle interactions. The mesoporosity of these supercrystals was confirmed by infiltrating H_2PdCl_4 into the supercrystal interior and reducing the precursor to form Pd nanoparticles. The simple preparation of these supercrystals should be readily scaled up to produce uniform distribution of gold supercrystals on an electrode surface to make modified electrodes. They may also be highly sensitive substrates for surface-enhanced Raman spectroscopic detection of trace molecules.[23] The mesoporosity displayed in some supercrystals implies that they may be used as regulated catalyst supports and for molecular and ion sensing. Infiltration of the interior pore channels with another material can easily produce highly structured composites. From a more fundamental perspective, this study shows that a better understanding of the general mechanism leading to supercrystal formation by polyhedral nanocrystals is essential.

■ ASSOCIATED CONTENT

Ⓢ Supporting Information

Additional experimental procedures, photographs of TXM sample holder, additional SEM image of the various supercrystals, optical images of the supercrystals, EDS spectrum, GC−MS spectra, and movies showing the supercrystal formation process. This material is available free of charge via the Internet at http://pubs.acs.org.

AUTHOR INFORMATION

Corresponding Author

hyhuang@mx.nthu.edu.tw.

Notes

The authors declare no competing financial interest.

ACKNOWLEDGMENTS

REFERENCES

(1) Nie, Z.; Petukhova, A.; Kumacheva, E. *Nat. Nanotechnol.* **2010**, *5*, 15−25.

(2) Kinge, S.; Crego-Calama, M.; Reinhoudt, D. N. *ChemPhysChem* **2008**, *9*, 20−42.

(3) Bigioni, T. P.; Lin, X.-M.; Nguyen, T. T.; Corwin, E. I.; Witten, T. A.; Jaeger, H. M. *Nat. Mater.* **2006**, *5*, 265−270.

(4) Chen, C.-F.; Tzeng, S.-D.; Chen, H.-Y.; Lin, K.-J.; Gwo, S. *J. Am. Chem. Soc.* **2008**, *130*, 824−826.

(5) Macfarlane, R. J.; Lee, B.; Jones, M. R.; Harris, N.; Schatz, G. C.; Mirkin, C. A. *Science* **2011**, *334*, 204−208.

(6) Shevchenko, E. V.; Talapin, D. V.; Murray, C. B.; O'Brien, S. *J. Am. Chem. Soc.* **2006**, *128*, 3620−3637.

(7) Shevchenko, E. V.; Talapin, D. V.; Kotov, N. A.; O'Brien, S.; Murray, C. B. *Nature* **2006**, *439*, 55−59.

(8) Redl, F. X.; Cho, K.-S.; Murray, C. B.; O'Brien, S. *Nature* **2003**, *423*, 968−971.

(9) Evers, W. H.; Nijs, B. D.; Filion, L.; Castillo, S.; Dijkstra, M.; Vanmaekelbergh, D. *Nano Lett.* **2010**, *10*, 4235−4241.

(10) Evers, W. H.; Friedrich, H.; Filion, L.; Dijkstra, M.; Vanmaekelbergh, D. *Angew. Chem., Int. Ed.* **2009**, *48*, 9655−9657.

(11) Tao, A.; Sinsermsuksakul, P.; Yang, P. *Nat. Nanotechnol.* **2007**, *2*, 435−440.

(12) Henzie, J.; Grünwald, M.; Widmer-Cooper, A.; Geissler, P. L.; Yang, P. *Nat. Mater.* **2012**, *11*, 131−137.

(13) Zhang, J.; Luo, Z.; Quan, Z.; Wang, Y.; Kumbhar, A.; Smilgies, D.-M.; Fang, J. *Nano Lett.* **2011**, *11*, 2912−2918.

(14) Ming, T.; Kou, X.; Chen, H.; Wang, T.; Tam, H.-L.; Cheah, K.-W.; Chen, J.-Y.; Wang, J. *Angew. Chem., Int. Ed.* **2008**, *47*, 9685−9690.

(15) Chang, C.-C.; Wu, H.-L.; Kuo, C.-H.; Huang, M. H. *Chem. Mater.* **2008**, *20*, 7570−7574.

(16) Quan, Z.; Fang, J. *Nano Today* **2010**, *5*, 390−411.

(17) Wu, J.-K.; Lyu, L.-M.; Liao, C.-W.; Wang, Y.-N.; Huang, M. H. *Chem.—Eur. J.* **2012**, *18*, 14473−14478.

(18) Wang, T.; Wang, X.; LaMontagne, D.; Wang, Z.; Wang, Z.; Cao, Y. C. *J. Am. Chem. Soc.* **2012**, *134*, 18225−18228.

(19) Alvarez-Puebla, R. A.; Agarwal, A.; Manna, P.; Khanal, B. P.; Aldeanueva-Potel, P.; Carbó-Argibay, E.; Pazos-Pérez, N.; Vigderman, L.; Zubarev, E. R.; Kotov, N. A.; Liz-Marzán, L. M. *Proc. Natl. Acad. Sci. U.S.A.* **2011**, *108*, 8517−8161.

(20) Xie, S.; Zhou, X.; Han, X.; Kuang, Q.; Jin, M.; Jiang, Y.; Xie, Z.; Zheng, L. *J. Phys. Chem. C* **2009**, *113*, 19107−19111.

(21) Shen, X. S.; Wang, G. Z.; Hong, X.; Zhu, W. *CrystEngComm* **2009**, *11*, 753−755.

(22) Demortière, A.; Launois, P.; Goubet, N.; Albouy, P.-A.; Petit, C. *J. Phys. Chem. B* **2008**, *112*, 14583−14592.

(23) Zhu, Z.; Meng, H.; Liu, W.; Liu, X.; Gong, J.; Qiu, X.; Jiang, L.; Wang, D.; Tang, Z. *Angew. Chem., Int. Ed.* **2011**, *50*, 1593−1596.

(24) Wu, H.-L.; Kuo, C.-H.; Huang, M. H. *Langmuir* **2010**, *26*, 12307−12313.

(25) Chung, P.-J.; Lyu, L.-M.; Huang, M. H. *Chem.—Eur. J.* **2011**, *17*, 9746−9752.

(26) Yunker, P. J.; Still, T.; Lohr, M. A.; Yodh, A. G. *Nature* **2011**, *476*, 308−311.

(27) Shulga, O. V.; Jefferson, K.; Khan, A. R.; D'Souza, V. T.; Liu, J.; Demchenko, A. V.; Stine, K. J. *Chem. Mater.* **2007**, *19*, 3902−3911.

(28) Ho, J.-Y.; Huang, M. H. *J. Phys. Chem. C* **2009**, *113*, 14159−14164.

(29) Lyu, L.-M.; Wang, W.-C.; Huang, M. H. *Chem.—Eur. J.* **2010**, *16*, 14167−14174.

(30) Gómez-Graña, S.; Hubert, F.; Testard, F.; Guerrero-Martínez, A.; Grillo, I.; Liz-Marzán, L. M.; Spalla, O. *Langmuir* **2012**, *28*, 1453−1459.

(31) Damasceno, P. F.; Engel, M.; Glotzer, S. C. *Science* **2012**, *337*, 453−457.

(32) Smallenburg, F.; Filion, L.; Marechal, M.; Dijkstra, M. *Proc. Natl. Acad. Sci. U.S.A.* **2011**, *109*, 17886−17890.

(33) Torquato, S.; Jiao, Y. *Nature* **2009**, *460*, 876−879.

(34) Huo, Q.; Margolese, D. I.; Ciesla, U.; Demuth, D. G.; Feng, P.; Gier, T. E.; Sieger, P.; Firouzi, A.; Chmelka, B. F. *Chem. Mater.* **1994**, *6*, 1176−1191.

(35) Gu, D.; Bongard, H.; Meng, Y.; Miyasaka, K.; Terasaki, O.; Zhang, F.; Deng, Y.; Wu, Z.; Feng, D.; Fang, Y.; Tu, B.; Schüth, F.; Zhao, D. *Chem. Mater.* **2010**, *22*, 4828−4833.

(36) Xia, Y.; Mokaya, R. *J. Mater. Chem.* **2003**, *13*, 657−659.

(37) Kuo, C.-H.; Chu, Y.-T.; Song, Y.-F.; Huang, M. H. *Adv. Funct. Mater.* **2011**, *21*, 792−797.

2693

dx.doi.org/10.1021/ja311008r | *J. Am. Chem. Soc.* 2013, 135, 2684−2693